RESEARCH ARTICLE

ADVANCED FUNCTIONAL MATERIALS

www.afm-journal.de

Generation and Detection of Dresselhaus-Like Spin Current in a Single-Crystal Ferromagnetic Metal

Wentao Wang, Ze Yan, Yang Cao, Cunxu Gao, Zhong Shi, Mingsu Si, Jiangwei Cao, Li Xi, Dezheng Yang, and Desheng Xue**

Distinct from the existing spin–orbit torque devices to only generate Rashba-like spin current, it is proposed to generate Dresselhaus-like spin current based on a single-crystal ferromagnetic metal. By employing the second harmonic Hall measurement, it is found that the second harmonic Hall signal in single-crystal ferromagnet exhibits an antisymmetric angular dependence induced by Dresselhaus-like spin current, opposite to the reported symmetric angular dependence induced by Rashba-like spin current. Such anomalous Dresselhaus-like spin current is further confirmed by the current-induced shift of the hysteresis loop when the magnetic field is swept along the current direction. However, when the ferromagnetic metal exhibits amorphous crystal structure or polycrystal structure, the Dresselhaus-like spin current is absent. This result complements the missing type of spin currents due to charge-to-spin conversion and benefits the formulation of comprehensive spin–orbit coupling mechanism, by considering additional broken symmetry caused by ferromagnetic order and the structure symmetry of the crystalline lattice.

1. Introduction

Spin currents converted by the charge currents in materials with large spin–orbit coupling have drawn great attention, which can exert spin–orbit torques (SOTs) to electrically manipulate nanomagnet.[1,2] Since the spin polarization carried by the spin current directly determines SOTs direction,[3,4] spin polarization has become a key parameter to optimize the SOT-induced magnetization dynamics, which would benefit the enhancement of SOT efficiency and the field-free switching.[5,6] However, considering spin current originating from either the spin Hall effect (SHE) or the Rashba effect,[7–10] it always requires that spin polarization, spin current flow, and charge current are orthogonal to each other. As a result, the spin polarization for conventional charge-to-spin conversion is only fixed along y-direction, as shown in **Figure 1**a.

To overcome the above limitation, the recent experiments and theories suggest two promising approaches to manipulate the polarization of the spin current. One is to use the low-symmetry point group of crystalline lattices.[11–13] In 2D Weyl semimetals WTe_2[11] and $MoTe_2$[12] as well as single-crystal heavy metal (HM) CuPt alloy,[13] the z-polarized spin current illustrated in Figure 1b can be obtained, by adjusting the relative orientation between charge current and high-symmetry axis. The other one is to employ the magnetic order.[14–25] The pure ferromagnet (FM) material can be naturally served as spin current source of the z-polarized spin current,[14,15] because the system symmetry can be broken by the FM magnetization. Even if neglecting intrinsic contributions to both SHE and Rashba effect, the z-polarized spin current in FM/nonmagnetic interface is still predicated due to the interface spin current effect,[16,17] and soon is observed in FM/light metal (LM) multilayers.[18–21] Besides FM order, antiferromagnet (AFM) order can also be used to modulate the polarization of spin current based on the same reason, named magnetic SHE.[22] The z-polarized spin current has been observed, not only in non-collinear AFM with broken spin conservation,[23] but also in collinear AFM with spin conservation.[24,25] However, no matter the y-polarized spin current (Figure 1a) or the z-polarized spin current (Figure 1b), the spin polarization for generated spin current is still perpendicular to the charge current, referred to as Rashba-like spin current, the Dresselhaus-like spin current as shown in Figure 1c that spin polarization is parallel to charge current is still difficult to be generated due to the limitation of the symmetry. The finding of Dresselhaus-like spin current is useful for the formulation of comprehensive charge-to-spin conversion mechanism and for developing potential SOT devices with higher efficiency.

Despite the microscopic mechanisms to manipulate the polarization of spin current being complex, it is generally accepted that the key factor to modulate the spin polarization is

W. Wang, Z. Yan, Y. Cao, C. Gao, M. Si, J. Cao, L. Xi, D. Yang, D. Xue
Key Laboratory for Magnetism and Magnetic Materials of Ministry of Education
Lanzhou University
Lanzhou 730000, China
E-mail: yangdzh@lzu.edu.cn; xueds@lzu.edu.cn

W. Wang
Institute of Modern Physics
Chinese Academy of Science
Lanzhou 730000, China

Z. Shi
Shanghai Key Laboratory of Special Artificial Microstructure and School of Physics Science and Engineering
Tongji University
Shanghai 200092, China

The ORCID identification number(s) for the author(s) of this article can be found under https://doi.org/10.1002/adfm.202204212.

DOI: 10.1002/adfm.202204212

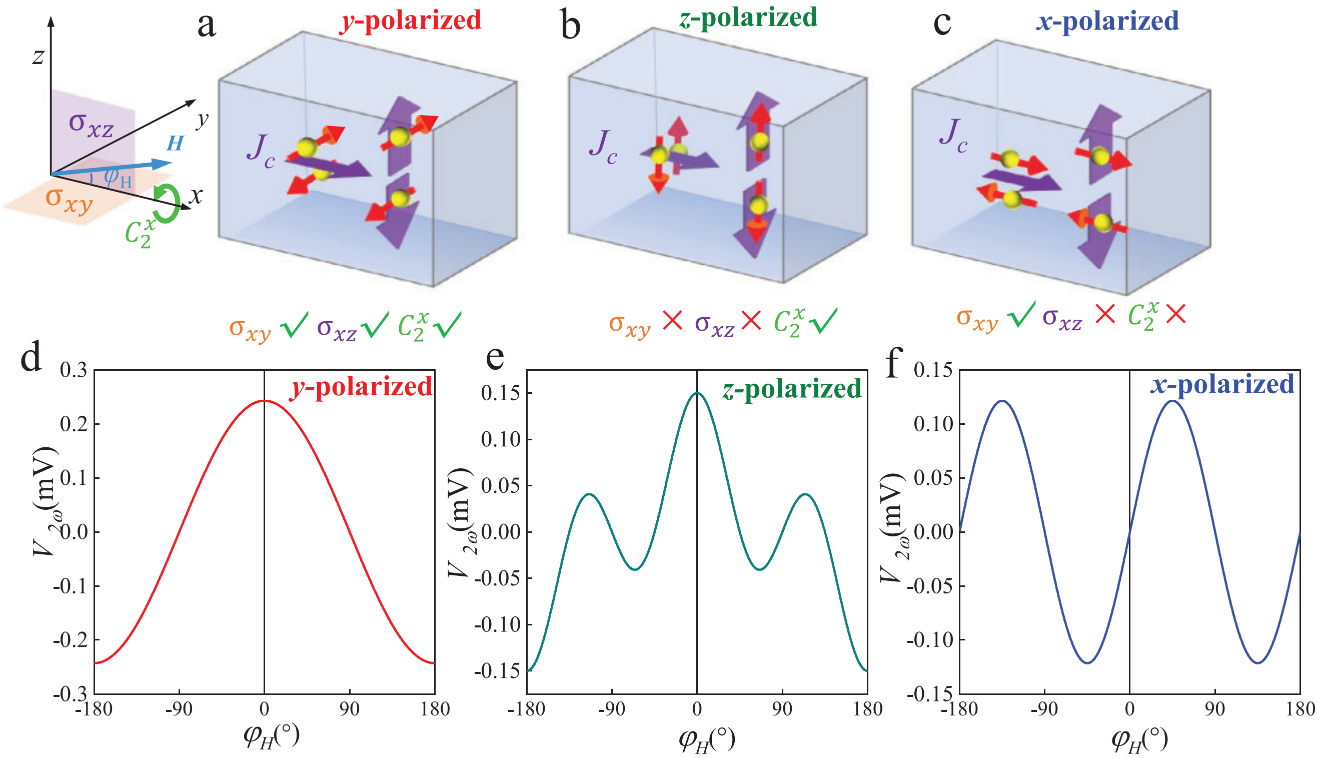

Figure 1. Schematic diagram of the symmetry-dependent spin current with different polarization. a–c) Three possible polarizations (*y*, *z*, and *x*) carried by out-of-plane spin currents, respectively. When charge current J_c is passed along the *x* axis, the system still reserves two mirror symmetries σ_{xy} and σ_{xz}, as well as the twofold rotational symmetry C_x^2. Unlike *z*- and *x*-polarized spin currents that can only satisfy symmetries C_x^2 and σ_{xy}, respectively, *y*-polarized spin current can satisfy all these three symmetries. This indicates that the *y*-polarized spin current can be generated by the *x*-direction charge current for high-symmetry system, while the *z*- or the *x*-polarized spin current can only occur at symmetry-reduced system, where the limitations of symmetry conditions are broken. d–f) The calculated angular dependence of $V_{2\omega}$ induced by the damping-like torque for the *y*-, the *z*-, or the *x*- polarized spin current according to the macro spin model, respectively, where magnetic field *H* is rotated in *xy* plane. Under mirror symmetry operation σ_{yz}, *y*- and *z*- polarized spin currents are opposite, but *x*-polarized spin current is the same. This indicates that the angular dependence of $V_{2\omega}$ induced by the *y*- or the *z*- polarized spin currents are symmetric, while antisymmetric induced by *x*-polarized spin current, which is consistent with the calculation results.

the symmetry broken. As shown in Figure 1, for a system with high symmetry, charge current would make the system preserve two mirror symmetries σ_{xy} and σ_{xz}, as well as the twofold rotational symmetry along the *x*-axis C_x^2. According to the Curie principle,[26,27] the generated out-of-plane spin current should retain the same symmetries as charge current does. Thus, only the *y*-polarized spin current can satisfy these symmetry conditions. However, if such symmetries are broken, for instance, by the structure symmetry of the crystalline lattice or the magnetic order parameter, *z*- and even *x*-polarized (Dresselhaus-like) spin currents can be expected to occur.

In this work, we propose to generate the Dresselhaus-like spin current in a single-crystal FM thin film with in-plane magnetization, by the combination of the low-symmetry point group of crystalline lattices and the FM order together. Both symmetry analysis and macro spin model calculation show that the second harmonic Hall voltage $V_{2\omega}$ induced by the Dresselhaus-like spin current exhibits an antisymmetric angular dependence in *xy* plane, which contrasts to the conventional symmetric angular dependence induced by the *y*- or the *z*-polarized spin current, serving as a fingerprint for experiment detection and calibration. The *x*-polarized spin current is exponentially decayed with the thickness of FM, indicating a strong interface effect. By further inserting an epitaxial V layer to modify the FM interface, the *x* polarized spin current can increase one order of amplitude. The ability to generate the arbitrary *x*-, *y*- and *z*-polarized spin current will benefit designing of the more efficient SOT devices.

2. Results

2.1. Symmetry Analysis of $V_{2\omega}$

To measure the SOTs produced by spin currents with different polarizations, we use the technique of in-plane second harmonic Hall voltage,[28–30] performed at room temperature. An in-plane alternating current (a.c.) current of frequency ω is applied through the single FM layer to modulate the SOTs amplitudes and induce a small oscillation of magnetization away from its equilibrium direction. As a result, $V_{2\omega}$ is generated due to the variation of Hall resistance induced by magnetization oscillation. By rotating an applied in-plane magnetic field *H* with the azimuthal angle ϕ_H, $V_{2\omega}$ will present the specified geometric symmetry regarding the polarization of spin current. This is because under the mirror reflection σ_{yz}, the *y*- or the z-polarized spin current is reverted, however, the x-polarized spin current is the same. This also indicates that under the mirror reflection σ_{yz}, $V_{2\omega}$ produced by the y- or z-polarized spin current has the opposite symmetry to that produced by the x-polarized spin current, which reads

$$V_{2\omega}(\varphi_H) = \varepsilon V_{2\omega}(-\varphi_H) \tag{1}$$

where $\varepsilon = \pm 1$. For the y- and z-polarized spin current, $\varepsilon = +1$, giving rise to a symmetric angular dependence, as shown in Figures 1d,e, respectively. However, for the x-polarized spin current, $\varepsilon = -1$, giving rise to an antisymmetric angular dependence, as shown in Figure 1f. In Figure S1, Supporting Information, by using macro spin model, we derive the general expressions of $V_{2\omega}^{\sigma}$ produced by damping-like torque for spin current with spin polarization $\boldsymbol{\sigma} = y$, z, and x,

$$V_{2\omega} = \frac{1}{2} I_0 R_{\mathrm{AHE}} \frac{H_{\mathrm{DL}}}{H_{\mathrm{K}} + H} \cos\varphi_H - I_0 R_{\mathrm{PHE}} \frac{H_{\mathrm{FL}}}{H} \cos\varphi_H \cos 2\varphi_H \tag{2}$$

$$V_{2\omega} = \frac{1}{2} I_0 R_{\mathrm{AHE}} \frac{H_{\mathrm{FL}}}{H_{\mathrm{K}} + H} \cos\varphi_H + I_0 R_{\mathrm{PHE}} \frac{H_{\mathrm{DL}}}{H} \cos\varphi_H \cos 2\varphi_H \tag{3}$$

$$V_{2\omega} = -\frac{1}{4} I_0 R_{\mathrm{AHE}} \frac{H_{\mathrm{DL}}}{H_{\mathrm{K}} + H} \sin 2\varphi_H + \frac{1}{4} I_0 R_{\mathrm{PHE}} \frac{H_{\mathrm{FL}}}{H} \sin 4\varphi_H \tag{4}$$

where I_0 is the amplitude of charge current, R_{AHE} is the Hall resistance from the anomalous Hall effect (AHE), R_{PHE} is the Hall resistance from the planar Hall effect (PHE), H_{K} is the effective perpendicular anisotropy field, H_{DL} and H_{FL} are the effective field of damping-like torque and field-like torque. Obviously, the angular dependence of $V_{2\omega}$ produced by the spin current in Equations (2)–(4) can agree well with the symmetric relationship of Equation (1).

2.2. Crystal Structure and Device Configuration

Figure 2a displays a schematic of the device structure and the harmonic Hall voltage measurement configuration. The heterostructure V (t_{V} = 0–10.7 nm)/$Fe_{0.5}Co_{0.5}$(3.7 nm)/AlO_x on MgO (001) was fabricated by the molecular beam epitaxy (MBE) system under a base pressure of 5×10^{-11} mbar. Nucleation and growth are monitored in situ by reflection high energy electron diffraction pattern (RHEED) (Figure S2, Supporting Information). A 1.5-nm-thick Al is capped to prevent oxidation in the air. To measure the symmetry-dependent x-polarized spin current, the films were patterned to 10 µm wide Hall bar along with different directions (θ_{I}) with respect to the MgO [100] direction (Figure 2b) by optical lithography technology.

The crystal structure and orientation of the heterostructure are investigated by X-ray diffraction (XRD). The θ–2θ XRD curve of V/$Fe_{0.5}Co_{0.5}$ in Figure 2c clearly shows V (002) peaks at $2\theta = 60.0°$ and $Fe_{0.5}Co_{0.5}$ (002) peaks at $2\theta = 66.5°$, indicating the out-of-plane lattice constants are 0.31 and 0.28 nm, respectively. The φ scans of $Fe_{0.5}Co_{0.5}$ (202) and MgO (202) plane without other detectable phases are shown in Figure 2d. The same height and fourfold symmetry of $Fe_{0.5}Co_{0.5}$ (202) peak further prove a very high-quality single-crystal thin film. The relative positions of $Fe_{0.5}Co_{0.5}$ (202) peak and MgO (202) peak also verify that the epitaxial bcc structures of V and FeCo layers are rotated 45° with respect to that of MgO substrate, as shown in Figure 2b. The cross-sectional high-resolution transmission electron microscopy (HR-TEM) image shows an atomically sharp boundary between

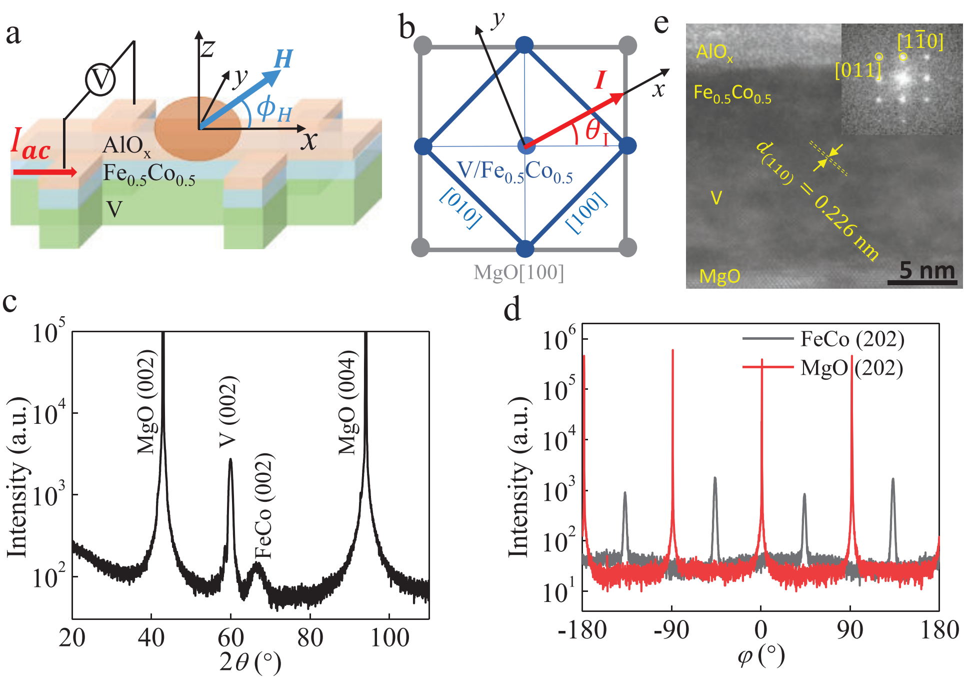

Figure 2. Structural characterization. a) The schematic of the device structure and the harmonic Hall voltage measurement. b) The schematic of epitaxial crystalline structure for the MgO/V/$Fe_{0.5}Co_{0.5}$/AlO_x heterostructure in xy plane. θ_{I} represents the longitudinal direction of Hall bar, and the x-axis is defined as the direction of the charge current. c,d) The corresponding θ–2θ scanning and φ scanning of XRD curves. e) The corresponding TEM image.

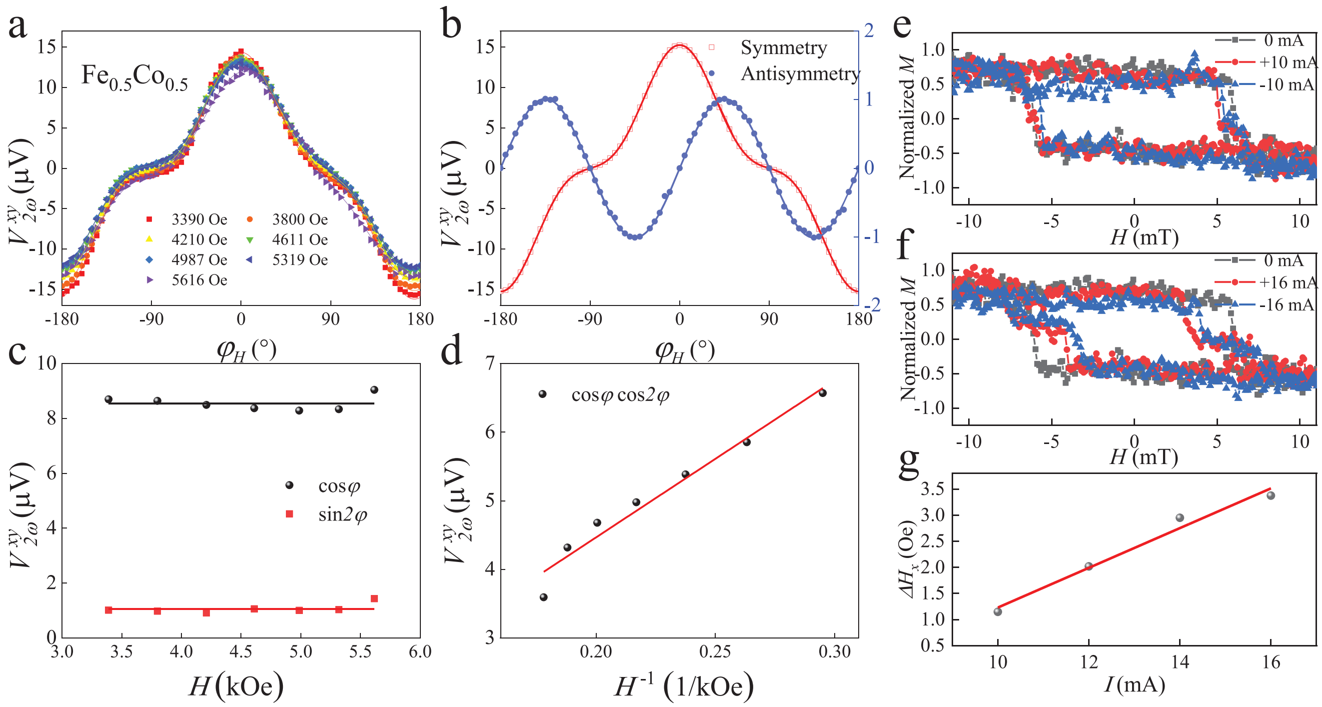

Figure 3. Quantitative determination and characterization of SOT induced by x-polarized spin current. a) The angular dependence of $V_{2\omega}$ under various magnetic fields H. b) The decoupled symmetric and asymmetric angular components of $V_{2\omega}$. The antisymmetric component is fitted very well by $\sin2\phi_H$, indicating the existence of x-polarized spin current. c) The amplitudes of $\cos\phi_H$ and $\sin2\phi_H$ terms as a function of H. d) The amplitude of $\cos\phi_H \cos2\phi_H$ term as a function of H^{-1}. The hysteresis loops of MgO/V (8.8 nm)/$Fe_{0.5}Co_{0.5}$ device under e) $I = \pm10$ mA, f) $I = \pm16$ mA,respectively. g) The current dependence of the hysteresis loop shift along the x-direction.

each layer, as shown in Figure 2e. This exhibits the epitaxial relationship with MgO(001)[100]||FeCo(001)[110] and similar lattice constant, which are consistent with the XRD results.

2.3. Evidence of x-Polarized Spin Current

Figure 3a shows that the angular dependence of $V_{2\omega}^{xy}$ of MgO/$Fe_{0.5}Co_{0.5}$(3.7 nm)/AlO_x heterostructure is asymmetric. According to the above discussion, the angular dependence of $V_{2\omega}^{xy}$ for y- or z-polarized spin current should be symmetric, the antisymmetric angular dependence of $V_{2\omega}^{xy}$ indicates the presence of an anomalous SOT induced by x-polarization spin current. To demonstrate it, the antisymmetric component is directly abstracted by $\frac{1}{2}(V_{2\omega}(\varphi_H) - V_{2\omega}(-\varphi_H))$, as shown in Figure 3b. One can find that it can be fitted very well by $\sin2\phi_H$, which obeys with damping-like term in Equation (4). Since H_K (≈2.2 T) is much larger than H, the amplitude of $\sin2\phi_H$ terms are almost independent of H in Figure 3c. Thus, we can obtain the current-induced effective damping-like field for the x-polarized spin current, $H_{DL}/J_c = 3.1 \times 10^{-11}$ Oe $(Am^{-2})^{-1}$. The symmetric components can be described well by the functions of $\cos\phi_H$ and $\cos2\phi_H \cos\phi_H$ that arises from y- or z-polarized spin currents. Consistent with Equation (2), the amplitude of $\cos\phi_H$ term in Figure 3c is almost independent of H, as shown in Figure 3c, whereas the amplitude of $\cos\phi_H \cos2\phi_H$ term in Figure 3d is proportional to H^{-1}, which agrees with Equation (3). Remarkably, the angular dependencies of symmetric components of $V_{2\omega}^{xy}$ in our single FM layer are consistent with that in HM/FM bilayers.[28–30] In the conventional HM/FM bilayer SOT device, the spin current is generated by HM and its interface, while, in our case, the spin current is generated by FM interface or the bulk FM itself.[31–33] Moreover, the x-polarization spin current can also be confirmed by current-induced shift of the hysteresis loop. When a direct current (d.c.) current is applied into the Hall bar, the x-polarized spin current can generate the x-direction effective field to shift the hysteresis loops. As shown in Figure 3e, when positive (+10 mA) and negative (–10 mA) currents are applied to the Hall bar, the x-direction hysteresis loop for MgO/V(8.8 nm)/$Fe_{0.5}Co_{0.5}$ device is slightly shifted toward opposite directions. However, as current increases to 16 mA as shown in Figure 3f, the shift becomes more significant, despite the heat effect strongly shrinks the hysteresis loop. To characterize the x-polarized spin current, the shift field ΔH_x is defined by $(H_+(M = 0) - H_-(M = 0))/2$, where $H_+(M = 0)$ is the switching field at positive field range, and $H_-(M = 0)$ is the switching field at negative range. By linear fitting the current dependence of ΔH_x in Figure 3g, we estimate the current-induced effective field efficiency $\Delta H_x/J_C = 1.9 \times 10^{-10}$ Oe $(Am^{-2})^{-1}$, which is comparable with the 1.8×10^{-10} Oe $(Am^{-2})^{-1}$ obtained from the second harmonic Hall measurement.

2.4. The Analysis of Thermal Effect

Next, we will exclude that the $\sin2\varphi_H$ angular dependence originates from the thermal effect. If considering the thermal

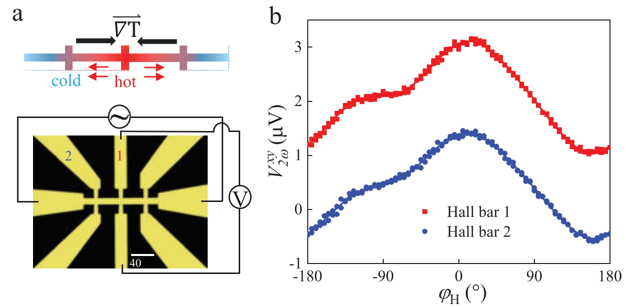

Figure 4. The analysis of in-plane thermal effect. a) The schematic illustration of in-plane thermal gradient for three-terminal Hall bar devices. b) The angular dependence of the second harmonic Hall voltage of MgO/FeCo(2)/AlO_x sample at Hall bar 1 (red curve) and Hall bar 2 (blue curve).

effect with vertical thermal gradients, the magneto-thermal effects, such as the anomalous Nernst effect[34–36] and spin Seebeck effect,[36–38] will yield $\cos\varphi_H$ angular dependence, not the observed $\sin2\varphi_H$ angular dependence. But if the thermal gradient is in-plane, where the large electrode can be considered as a heat sink as shown in **Figure 4**a, the second harmonic Hall signal due to the planar Nernst effect[36,39] indeed can yield a $\sin2\varphi_H$ angular dependence, but it should depend on the Hall bar positions. As shown in Figure 4b, the $V_{2\omega}^{xy}$ have the same angular dependences for the Hall bars, which can exclude that the observed $\sin2\varphi_H$ angular dependence originates from in-plane thermal gradients.

2.5. Impact of the Oersted Field

To check whether the current-induced Oersted field can cause the $\sin2\varphi_H$ angular dependence, a calibration experiment is carried out, by directly applying an in-plane a.c. Oersted field is perpendicular to the d.c. current as shown in **Figure 5**a. The amplitude of the a.c. Oersted field is about 3 Oe with frequency of 133 Hz. The d.c. current through MgO/$Fe_{0.5}Co_{0.5}$(3.7 nm)/AlO_x Hall bar device ($\theta_I = 0$) is 1 mA under the d.c. magnetic field H_{ext} = 3000 Oe. The first harmonic Hall voltage is acquired to measure angular dependence of $V_{1\omega}$ only induced by Oersted field. As shown in Figure 5b, the first harmonic Hall voltage is symmetric, the asymmetric $\sin2\phi_H$ term cannot be observed, where the symmetric and antisymmetric component is directly abstracted by $\frac{1}{2}(V_{2\omega}(\varphi_H)\pm V_{2\omega}(-\varphi_H))$, as shown in Figure 5c. More importantly, the curve can be well fitted by Equation (5), which only considers the a.c. Oersted field-induced magnetization oscillation.

$$V_{1\omega} = I_0 R_{PHE} \frac{H_{Oe}}{H} \cos\varphi_H \cos2\varphi_H \tag{5}$$

2.6. Impact of Crystal Structure

The observed $\sin2\varphi_H$ term depends strongly on the crystal structure, which is in stark contrast to the amorphous and polycrystal FM/HM scenario. In order to compare angular relation of second harmonic signal from amorphous, polycrystal, and single-crystal FM/HM, the amorphous Si/Ta(5)/CoFeB(3), polycrystal Si/Co(3)/Pt(5), and single-crystal MgO/FeSi/Pt samples with in-plane anisotropy are fabricated. The angular dependences of $V_{2\omega}^{xy}$ of Ta/CoFeB and Co/Pt samples as shown in **Figure 6**a,b are consistent with those reproducing known results,[28,29,40] where the only symmetric component is observed, and the antisymmetric component is absent, as

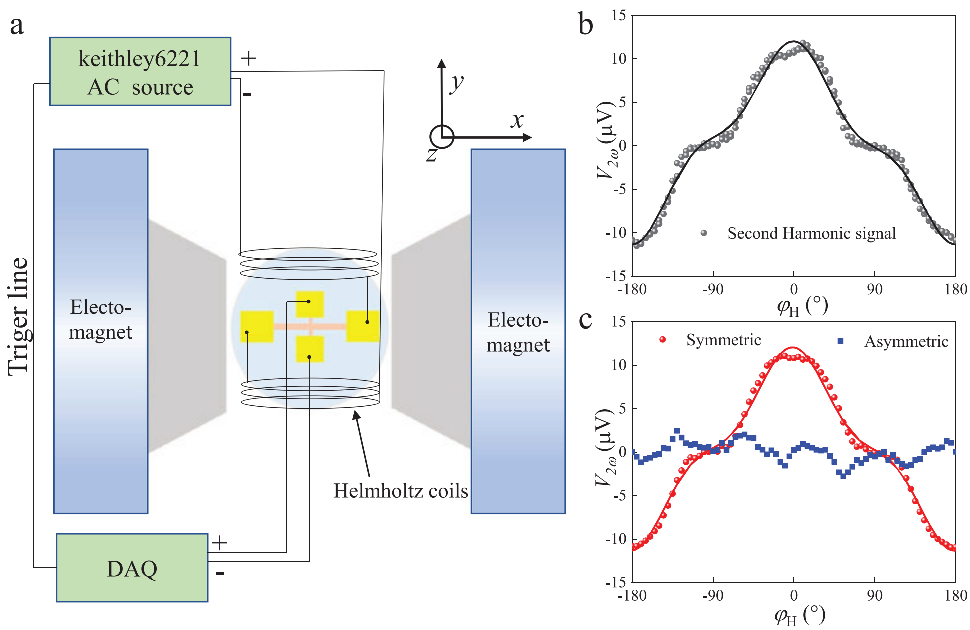

Figure 5. The calibration experiment of Oersted field. a) The schematic illustration of first harmonic measurement, where the amplitude of a.c. Oersted field is about 3 Oe with frequency of 133 Hz. b) The first harmonic Hall voltage signal by applying d.c. current with the amplitude of 0.5 mA under H = 3000 Oe for MgO/FeCo (3.7 nm)/AlO_x sample. c) The decoupled symmetric and asymmetric angular components of $V_{1\omega}$.

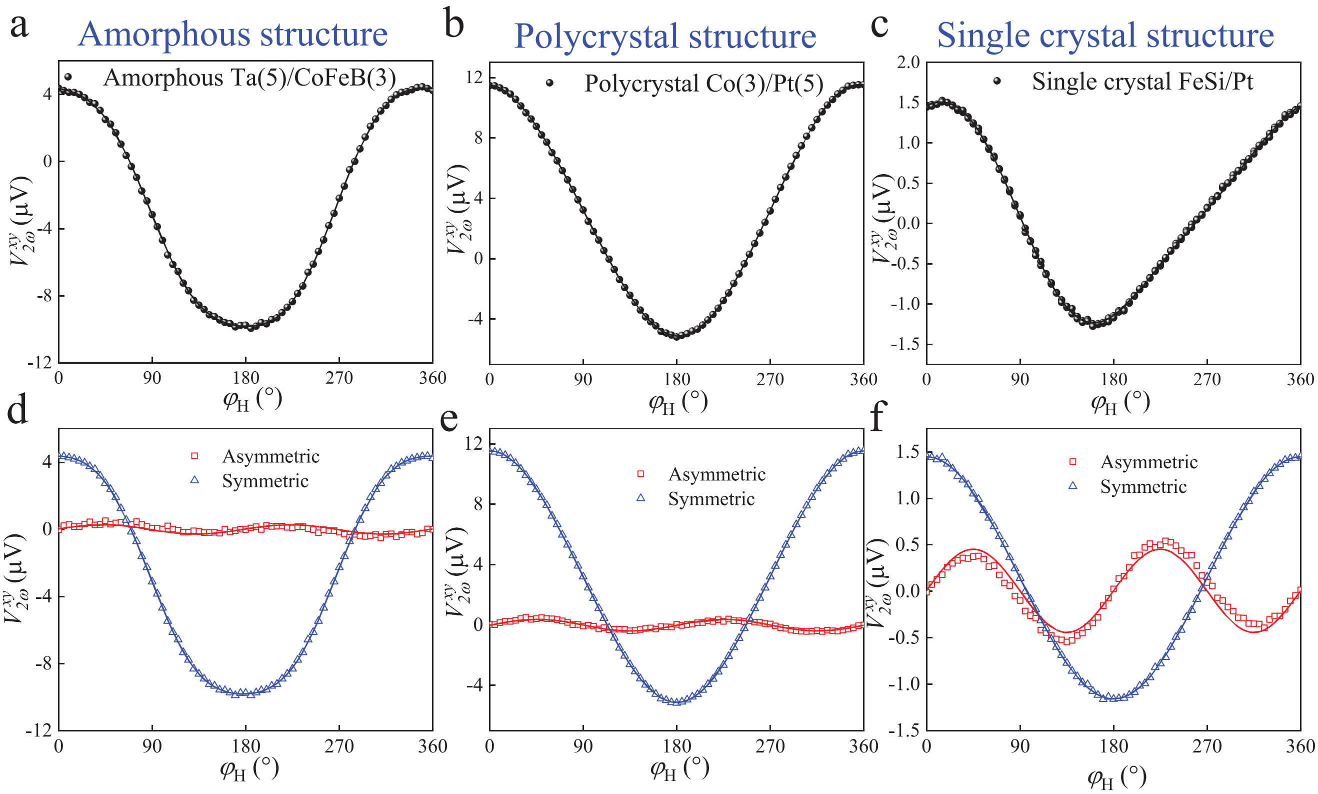

Figure 6. The Dresselhaus-like spin current depends on the crystal structure. The angular dependence of $V_{2\omega}^{xy}$ for a) Si/Ta(5)/CoFeB(3), b) Si/Co(3)/Pt(5), and c) single-crystal MgO/FeSi/Pt, and d–f) their corresponding extracted symmetric and asymmetric angular dependence of $V_{2\omega}^{xy}$.

shown in Figures 6d,e, respectively. However, for single-crystal FeSi, the asymmetric angular dependence of $V_{2\omega}^{xy}$ is still observed as shown in Figure 6c. Similar to the result of single-crystal $Fe_{0.5}Co_{0.5}$, the angular dependence for the single-crystal FeSi still concludes an additional antisymmetric angular component $\sin 2\varphi_H$, as shown in Figure 6f. These results not only support that the $\sin 2\varphi_H$ angular dependence strongly depends on the crystal structure of ferromagnetic films, but also suggest our method by using a single-crystal FM layer to generate the *x*-polarized spin current is generic.

2.7. Thickness Dependence of the *x*-Polarized Effective Field

To further understand the generation mechanism of *x*-polarized spin current, the typical angular dependence of $V_{2\omega}^{xy}$ with

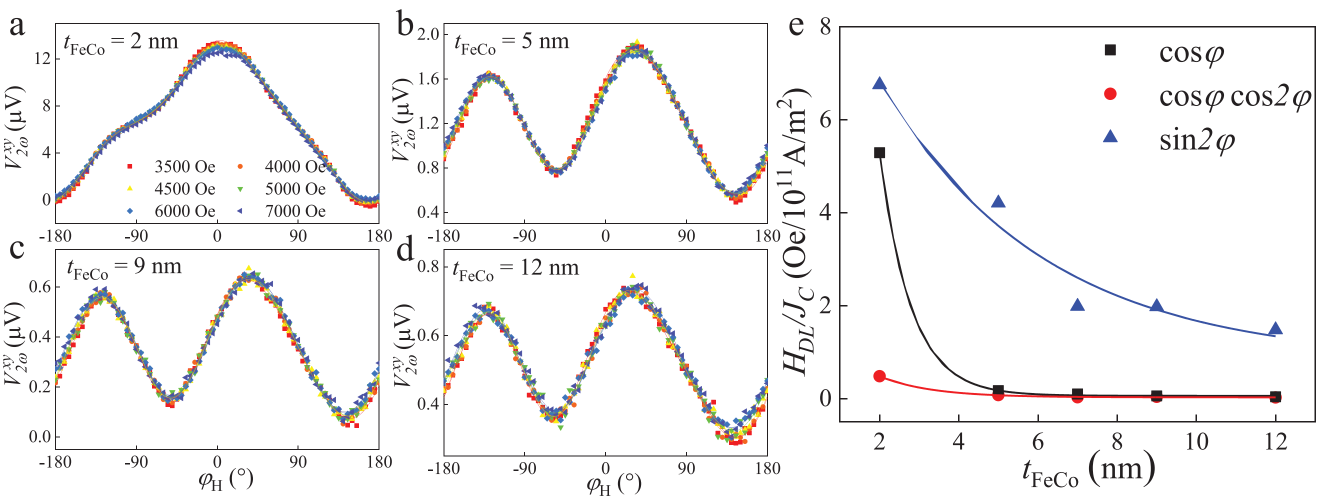

Figure 7. The FeCo thickness dependence of the spin current with various spin polarizations. a–d) The angular dependence of $V_{2\omega}$ of the epitaxial $MgO/Fe_{0.5}Co_{0.5}(t_{FeCo})/AlO_x$ with different t_{FeCo}. e) The fitted current-induced effective damping-like field as a function of t_{FeCo}.

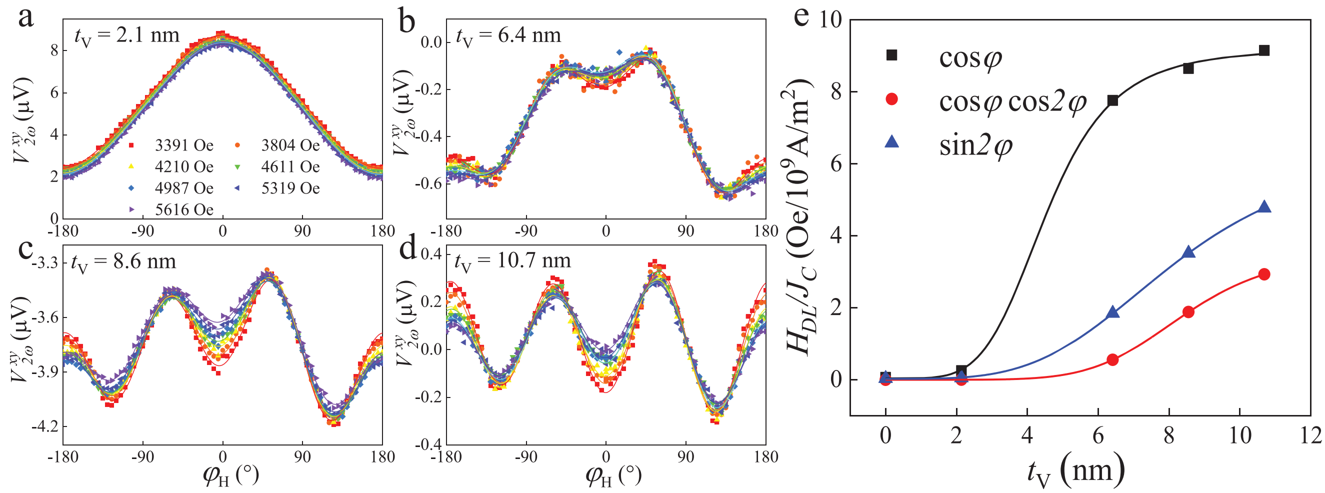

Figure 8. The interface-modulated-spin current with various spin polarizations. a–d) The angular dependence of $V_{2\omega}$ of the epitaxial MgO/V(t_V)/$Fe_{0.5}Co_{0.5}$(3.7)/AlO_x for different V layer thickness. e) The current-induced effective damping-like field for different polarized spin current of MgO/V(t_V)/$Fe_{0.5}Co_{0.5}$/AlO_x as a function of V thicknesses.

various FeCo thicknesses (t_{FeCo}) at I = 10 mA are shown in **Figure 7**. One can easily find that all the curves can be fitted very well by using Equations (2)–(4), as shown in Figure 7a–d. Moreover, Figure 7e further shows that as t_{FeCo} increases, the SOTs strongly decrease, indicating a strong interface effect.

2.8. Interface Modulation of the *x*-Polarized Effective Field

To further confirm that the *x*-polarized spin current originates from the interface effect, we will insert nonmagnetic metal with weak spin–orbit coupling, that is, V between MgO and FeCo layer to modify the interface. The typical angular dependence of $V_{2\omega}^{xy}$ in **Figure 8** demonstrates that the angular asymmetric component becomes more and more significant with increasing thickness of the V layer (t_V). For $t_V = 10.7$ nm, H_{DL}/J_c for the *x*-polarized spin current can be sharply increased up to 3.9×10^{-10} Oe $(\mathrm{Am}^{-2})^{-1}$, which is one order of magnitude larger than that of the single FeCo layer, as shown in Figure 8e. One important reason for the enhancement of *x*-polarized effective field is due to different interfacial potentials at V/FeCo interface and AlO_x/FeCo interface, which broke the C_2^x symmetry. Moreover, the dependences of the effective field induced by spin current with different polarization on θ_I show a twofold symmetry (Figure S8, Supporting Information). This indicates that the *x*-polarized spin current is significantly related to the symmetry of the FM crystalline lattices, which excludes that the enhancement of anomalous SOT is caused by orbit- Hall effect of V.[41,42]

3. Conclusion

In summary, we have demonstrated the generation of anomalous SOTs corresponding to the *x*-polarized spin current in an epitaxial single-crystal FM thin film, by both the second harmonic Hall measurement and the hysteresis loop shift under current along *x*-direction. Such *x*-polarized spin current can be widely observed in single-crystal $Fe_{0.5}Co_{0.5}$ and $Fe_{0.86}Si_{0.14}$ layers by controlling the crystalline symmetry and the FM order, but it is absent in amorphous FeCoB layer and polycrystal Co layer. This work provides essential insight into understanding how the *x*-polarized spin current can arise in a single-crystal FM thin film due to breaking symmetric conditions C_x^2 and σ_{xz}. The method by using single-crystal FM to generate spin current with arbitrary spin polarization will lead to a much more efficient manipulation and deterministic magnetization switching of nanomagnets. Our finding offers the possibility to design and control spin currents, which will open areas of research opportunities in single-crystal FM spintronics.

Supporting Information

Supporting Information is available from the Wiley Online Library or from the author.

Acknowledgements

W.W. and Z.Y. contributed equally to this work. Authors acknowledge Prof. Jin Xiaofeng for the helpful discussion. This work was supported by National Natural Science Foundation of China (Grant No. 11774139), National Natural Science Foundation of China (Grant No. 11874189), National Natural Science Foundation of China (Grant No. 91963201), Program for Changjiang Scholars and Innovative Research Team in University (Grant No. IRT-16R35), 111 Project under Grant No. B20063, and Fundamental Research Funds for the Central Universities lzujbky-2021-ct01.

Conflict of Interest

The authors declare no conflict of interest.

Data Availability Statement

The data that support the findings of this study are available from the corresponding author upon reasonable request.

Keywords

single-crystal ferromagnetic thin films, spin–orbit torque, symmetry broken

Received: April 14, 2022
Published online: June 10, 2022

[1] A. Manchon, J. Železný, I. M. Miron, T. Jungwirth, J. Sinova, A. Thiaville, K. Garello, P. Gambardella, *Rev. Mod. Phys.* **2019**, *91*, 035004.
[2] X. Qiu, Z. Shi, W. Fan, S. Zhou, H. Yang, *Adv. Mater.* **2018**, *30*, 1705699.
[3] I. M. Miron, K. Garello, G. Gaudin, P.-J. Zermatten, M. V. Costache, S. Auffret, S. Bandiera, B. Rodmacq, A. Schuhl, P. Gambardella, *Nature* **2011**, *476*, 189.
[4] L. Liu, C.-F. Pai, Y. Li, H. W. Tseng, D. C. Ralph, R. A. Buhrman, *Science* **2012**, *336*, 555.
[5] S. Fukami, C. Zhang, S. DuttaGupta, A. Kurenkov, H. Ohno, *Nat. Mater.* **2016**, *15*, 535.
[6] W. J. Kong, C. H. Wan, X. Wang, B. S. Tao, L. Huang, C. Fang, C. Y. Guo, Y. Guang, M. Irfan, X. F. Han, *Nat. Commun.* **2019**, *10*, 233.
[7] M. I. Dyakonov, V. I. Perel, *Phys. Lett. A* **1971**, *35*, 459.
[8] J. Sinova, S. O. Valenzuela, J. Wunderlich, C. H. Back, T. Jungwirth, *Rev. Mod. Phys.* **2015**, *87*, 1213.
[9] A. Hoffmann, *IEEE Trans. Magn.* **2013**, *49*, 5172.
[10] Y. Liu, G. Yu, *Nat. Electron.* **2019**, *2*, 555.
[11] D. MacNeill, G. M. Stiehl, M. H. D. Guimaraes, R. A. Buhrman, J. Park, D. C. Ralph, *Nat. Phys.* **2017**, *13*, 300.
[12] P. Song, C.-H. Hsu, G. Vignale, M. Zhao, J. Liu, Y. Deng, W. Fu, Y. Liu, Y. Zhang, H. Lin, V. M. Pereira, K. P. Loh, *Nat. Mater.* **2020**, *19*, 292.
[13] L. Liu, C. Zhou, X. Shu, C. Li, T. Zhao, W. Lin, J. Deng, Q. Xie, S. Chen, J. Zhou, R. Guo, H. Wang, J. Yu, S. Shi, P. Yang, S. Pennycook, A. Manchon, J. Chen, *Nat. Nanotechnol.* **2021**, *16*, 277.
[14] J. Sinova, D. Culcer, Q. Niu, N. A. Sinitsyn, T. Jungwirth, A. H. MacDonald, *Phys. Rev. Lett.* **2004**, *92*, 126603.
[15] H. Kurebayashi, J. Sinova, D. Fang, A. C. Irvine, T. D. Skinner, J. Wunderlich, V. Novák, R. P. Campion, B. L. Gallagher, E. K. Vehstedt, L. P. Zârbo, K. Výborný, A. J. Ferguson, T. Jungwirth, *Nat. Nanotechnol.* **2014**, *9*, 211.
[16] V. P. Amin, M. D. Stiles, *Phys. Rev. B* **2016**, *94*, 104420.
[17] V. P. Amin, J. Zemen, M. D. Stiles, *Phys. Rev. Lett.* **2018**, *121*, 136805.
[18] A. M. Humphries, T. Wang, E. R. J. Edwards, S. R. Allen, J. M. Shaw, H. T. Nembach, J. Q. Xiao, T. J. Silva, X. Fan, *Nat. Commun.* **2017**, *8*, 911.
[19] S. C. Baek, V. P. Amin, Y.-W. Oh, G. Go, S.-J. Lee, G.-H. Lee, K.-J. Kim, M. D. Stiles, B.-G. Park, K.-J. Lee, *Nat. Mater.* **2018**, *17*, 509.
[20] R. Wang, Z. Xiao, H. Liu, Z. Quan, X. Zhang, M. Wang, M. Wu, X. Xu, *Appl. Phys. Lett.* **2019**, *114*, 042404.
[21] W. S. Aljuaid, S. R. Allen, A. Davidson, X. Fan, *Appl. Phys. Lett.* **2018**, *113*, 122401.
[22] M. Kimata, H. Chen, K. Kondou, S. Sugimoto, P. K. Muduli, M. Ikhlas, Y. Omori, T. Tomita, A. H. MacDonald, S. Nakatsuji, Y. Otani, *Nature* **2019**, *565*, 627.
[23] T. Nan, C. X. Quintela, J. Irwin, G. Gurung, D. F. Shao, J. Gibbons, N. Campbell, K. Song, S.-Y. Choi, L. Guo, R. D. Johnson, P. Manuel, R. V. Chopdekar, I. Hallsteinsen, T. Tybell, P. J. Ryan, J.-W. Kim, Y. Choi, P. G. Radaelli, D. C. Ralph, E. Y. Tsymbal, M. S. Rzchowski, C. B. Eom, *Nat. Commun.* **2020**, *11*, 4671.
[24] X. Chen, S. Shi, G. Shi, X. Fan, C. Song, X. Zhou, H. Bai, L. Liao, Y. Zhou, H. Zhang, A. Li, Y. Chen, X. Han, S. Jiang, Z. Zhu, H. Wu, X. Wang, D. Xue, H. Yang, F. Pan, *Nat. Mater.* **2021**, *20*, 800.
[25] R. González-Hernández, L. Šmejkal, K. Výborný, Y. Yahagi, J. Sinova, T. Jungwirth, J. Železný, *Phys. Rev. Lett.* **2021**, *126*, 127701.
[26] A. F. Chalmers, *Brit. J. Phil. Sci.* **1970**, *21*, 133.
[27] A. Davidson, V. P. Amin, W. S. Aljuaid, P. M. Haney, X. Fan, *Phys. Lett. A* **2020**, *384*, 126228.
[28] M. Hayashi, J. Kim, M. Yamanouchi, H. Ohno, *Phys. Rev. B* **2014**, *89*, 144425.
[29] C. O. Avci, K. Garello, M. Gabureac, A. Ghosh, A. Fuhrer, S. F. Alvarado, P. Gambardella, *Phys. Rev. B* **2014**, *90*, 224427.
[30] Y. Wen, J. Wu, P. Li, Q. Zhang, Y. Zhao, A. Manchon, J. Q. Xiao, X. Zhang, *Phys. Rev. B* **2017**, *95*, 104403.
[31] T. Wang, W. Wang, Y. Xie, M. A. Warsi, J. Wu, Y. Chen, V. O. Lorenz, X. Fan, J. Q. Xiao, *Sci. Rep.* **2017**, *7*, 1306.
[32] W. Wang, T. Wang, V. P. Amin, Y. Wang, A. Radhakrishnan, A. Davidson, S. R. Allen, T. J. Silva, H. Ohldag, D. Balzar, B. L. Zink, P. M. Haney, J. Q. Xiao, D. G. Cahill, V. O. Lorenz, X. Fan, *Nat. Nanotechnol.* **2019**, *14*, 819.
[33] M. Jiang, H. Asahara, S. Sato, T. Kanaki, H. Yamasaki, S. Ohya, M. Tanaka, *Nat. Commun.* **2019**, *10*, 6.
[34] A. Sakai, Y. P. Mizuta, A. A. Nugroho, R. Sihombing, T. Koretsune, M.-T. Suzuki, N. Takemori, R. Ishii, D. Nishio-Hamane, R. Arita, P. Goswami, S. Nakatsuji, *Nat. Phys.* **2018**, *14*, 1119.
[35] M. Ikhlas, T. Tomita, T. Koretsune, M.-T. Suzuki, D. Nishio-Hamane, R. Arita, Y. Otani, S. Nakatsuji, *Nat. Phys.* **2017**, *13*, 1085.
[36] M. Schmid, S. Srichandan, D. Meier, T. Kuschel, J.-M. Schmalhorst, M. Vogel, G. Reiss, C. Strunk, C. H. Back, *Phys. Rev. Lett.* **2013**, *111*, 187201.
[37] H. Adachi, K. Uchida, E. Saitoh, S. Maekawa, *Rep. Prog. Phys.* **2013**, *76*, 036501.
[38] D. Qu, S. Y. Huang, J. Hu, R. Wu, C. L. Chien, *Phys. Rev. Lett.* **2013**, *110*, 067206.
[39] A. D. Avery, M. R. Pufall, B. L. Zink, *Phys. Rev. Lett.* **2012**, *109*, 196602.
[40] F. Luo, S. Goolaup, W. C. Law, S. Li, F. Tan, C. Engel, T. Zhou, W. S. Lew, *Phys. Rev. B* **2017**, *95*, 174415.
[41] H. Kontani, T. Tanaka, D. S. Hirashima, K. Yamada, J. Inoue, *Phys. Rev. Lett.* **2009**, *102*, 4.
[42] D. Jo, *Phys. Rev. B* **2018**, *98*, 11.